CrossMark

Processing maps for the analysis of hot workability of microalloyed steels 38MnSiVS5 and 0.39C1.47Mn

Rudimylla da Silva Septimio[1] · Sergio Tonini Button[1] · Chester John Van Tyne[2]

Abstract Microalloyed steels are gaining increasing importance as substitutions for carbon steels because they possess higher mechanical properties, such as strength and toughness after hot forging, without a need for post-deformation heat treatment. To increase machinability, sulfur is added to microalloyed steels to facilitate chip removal, increase productivity, and enhance the life of cutting tools. Otherwise, the sulfide particles that benefit machinability may cause a significant loss in hot workability. Therefore, it is important to understand the effect of initial grain size, phase constituents, and inclusion content on flow stresses during hot working in order to establish ideal processing conditions, which prevent the formation of defects and simultaneously improve mechanical properties. The aim of the current study is to construct processing maps to evaluate the hot workability of microalloyed steels DIN 38MnSiVS5 and 0.39C1.47Mn in order to define the constitutive behavior of both steels under hot working and identify the safe regions for metalworking. The processing maps for both steels showed a region of instability at temperatures between 1100 and 1150 °C and the highest strain rates (namely, 10.0 and 30.0 s^{-1}) that should be avoided. Cracks were found in the sample of 0.39C1.47Mn steel and voids were found in the central region in the DIN 38MnSiVS5 steel. These defects might be caused by MnS inclusions and are probably the cause of instability. Therefore, it can be concluded that a higher sulfur content has a negative effect on workability, and might be the cause of instability under some processing conditions.

Introduction

The use of microalloyed steels is a trend in the automotive industry as a substitute for steels that are conventionally used in engines, suspensions, and transmission parts. Microalloyed steels present similar (and in some cases, even superior) mechanical properties when compared to conventional steels; and more significantly, when direct-cooled from hot forging, they do not need any additional heat treatment like normalizing, which can facilitate the production of high-strength steel parts.

Bu et al. [1] studied how cooling rate could influence the precipitation of carbides in a Ti–Nb–Mo microalloyed steel immediately after hot working. They evaluated three rates (5.0, 1.0, and 0.5 °C/s) and concluded that increasing cooling rate causes the decrease of the volume fraction and size of the precipitates, that have great influence on the final mechanical properties.

Zhang et al. [2] evaluated a V–Ti–N high-strength microalloyed medium-carbon steel used for fracture splitting of connecting rods and concluded that the steel was constituted of ferrite and pearlite. They also observed that by reducing the finish rolling temperature and accelerating the cooling rate after rolling, a microstructure with fine grain ferrite and narrow lamellar space pearlite could be obtained with a large number of precipitated phases distributed over ferrite.

✉ Sergio Tonini Button
sergio1@fem.unicamp.br

Rudimylla da Silva Septimio
rudi_septimio@hotmail.com

Chester John Van Tyne
cvantyne@mines.edu

[1] School of Mechanical Engineering, University of Campinas, CP 6122, Campinas 13083-970, Brazil

[2] Department of Metallurgical and Materials Engineering, Colorado School of Mines, Golden 80401, USA

Due to their increasing applications, microalloyed steels have been studied intensively. Kim and Park [3] studied the Avrami kinetics of the dynamic recrystallization of a V-microalloyed medium-carbon steel with flow curves and analyzing the evolution of grain size distribution. They modeled the flow softening kinetics and flow curves under various deformation conditions and concluded that the softening fractions estimated from the flow curves tend to overestimate the dynamically recrystallized fractions at a later stage of deformation, where the kinetics of dynamic recrystallization appear to be retarded by dynamic precipitation.

The vanadium microalloyed steel (30MnSV6) was heat treated at different conditions by Hajisafari et al. [4], and the relationship between microstructural and mechanical properties was studied. They concluded that the best combination of properties is related with the pearlite interlamellar spacing and with the size of pre-eutectoid ferrite, as well as by the presence of (V,Ti)C and VC precipitates on the grain and sub-grain boundaries, or randomly distributed inside the pro-eutectoid ferrite phase.

Mejia et al. [5] performed the modeling of hot flow behavior for low-carbon advanced ultra-high strength steels (A-UHSS) that were microalloyed with different amounts of boron. The presence of boron in the steels decreases the apparent activation energy for recrystallization, which indicates that the addition of boron accelerates the onset of dynamic recrystallization (DRX).

Wei et al. [6] studied the effect of carbon content on the hot deformation behavior of vanadium microalloyed steels, and found that the addition of carbon could decrease the work hardening rate when deformed at lower strain rates and could also accelerate both the occurrence and the rate of dynamic recrystallization.

Processing maps have been extensively used to evaluate the hot workability of a wide variety of metal alloys under different processing conditions, but few works are available in recent literature that present processing maps of microalloyed steels. Some of the first results were shown by Prasad and Sasidhara [7] who elaborated a comprehensive compendium with processing maps for hot working of most important metallic alloys.

Omar et al. [8] analyzed the hot workability of a microalloyed medium-carbon steel using power dissipation maps that were based on a dynamic materials model (DMM), and concluded that the selected steel experimented dynamic recrystallization in the range of about 1150 °C and 10 s^{-1} and that dynamic recovery in the domain centered at about 900 °C and 0.1 s^{-1}, which may be considered to be the optimum processing region for hot working.

Gu et al. [9] used hot compression tests to investigate the behavior of 38MnVS6 non-quenched steel. It was found that unstable phenomena did not appear under the deformation conditions; however, the optimal parameters for hot working were in the temperature range of 950–1200 °C and the strain rate range from 0.01 to 5 s^{-1}, where the processing map exhibited a domain of complete dynamic recrystallization.

El Hassani et al. [10] investigated the deformation stability of a medium-carbon microalloyed steel during hot forging, using two different processing maps based on phenomenological and continuum criteria. The results showed that all instability maps at the strain of 0.6, which corresponds to the steady state and presents a domain of dynamic recrystallization, which the authors considered to be the optimum hot working domain. Both maps also presented a domain of recovery and no unstable flow.

Xu et al. [11] built processing maps for a medium-carbon V–N microalloyed steel (designated as VN steel) and a medium-carbon V–N bared steel (designated as non-VN steel). The aim of this investigation was to understand the hot deformation behavior and the influence of vanadium and nitrogen in the temperature range of 750–1100 °C and the strain rate range of 0.005–30 s^{-1}. They concluded that the addition and precipitation of vanadium and nitrogen carbides could hinder dynamic recrystallization, which is the reason why the VN steel has a higher critical strain for dynamic recrystallization and a higher peak stress, as compared to the non-VN steel.

Wei and Liu [12] analyzed the workability of a C-Mn steel and two Nb microalloyed steels through compression tests at temperatures ranging from 900 to 1100 °C and strain rates from 0.005 to 10 s^{-1}. They concluded that the addition of Nb can effectively increase the peak strain and steady state strain and delay the occurrence of dynamic recrystallization; while the addition of C reduces the characteristic strains of Nb microalloyed steels and consequently promotes the occurrence of dynamic recrystallization.

The DIN 38MnSiVS5 and 39C1.4Mn microalloyed steels in the current study have a significant amount of sulfur which is necessary to increase machinability and facilitate chip formation, as discussed by Stephenson and Agapiou [13] who concluded that the manganese sulfides formed in the steel could coat and lubricate the rake face of the cutting tool, reducing friction, tool–chip temperatures, and tool wear rates.

Small amounts of manganese are usually added in steels to form MnS, which presents a higher melting temperature than FeS, thus avoiding incipient fusion at the grain boundaries during hot working, as shown by Bramfitt and Benscoter [14].

The presence of a small amount of sulfur significantly affects alloy and microalloyed steels, because sulfide inclusions are formed, which can compromise the steel

properties. Opiela and Kamińska [15] studied the modification of the chemical composition of non-metallic inclusions by rare-earth elements (lanthanum, cerium, and neodymium) in two new microalloyed steels to be used in the production of hot forged components. They succeed in obtaining low concentration of sulfur and oxygen, and consequently a low fraction of non-metallic inclusions, which should favor the production of hot forgings with high strength and ductility.

Xiao et al. [16] analyzed the influence of sulfur content and sulfide shape on fracture ductility in the case hardening steel DIN 18CrNiMo7-6, testing two levels of sulfur content and four amounts of calcium. They found that the size and shape of sulfide inclusions are related to sulfur content and calcium treatment, while the volume fraction of sulfide inclusions is only dependent on sulfur content. As a consequence, the transverse ductility significantly decreased with increasing sulfur content, while the anisotropy of fracture ductility can be decreased to some extent by the effects of inclusion modification due to calcium treatment. This method of shape control for the sulfides in steels works well for nominal contents of sulfur in the steel. When additional sulfur is added for machinability purposes, calcium treatment may not be as effective.

Kizu and Urabe [17] showed that sulfur inclusions, such as MnS or Fe(Mn)S, can cause a discontinuity of the steel matrix, which increases its non-uniformity and influences its performance.

As a result, it is important to study the hot workability of microalloyed steels with higher sulfur contents to know the safe limits of hot deformation to avoid plastic instability or fracture.

A processing map is based on the principles of the dynamic material model (DMM), which was developed by Prasad et al. [18] and describes the dynamic response of the material in terms of microstructural evolution under the imposed processing conditions, as shown by Lenz et al. [19] who analyzed the plastic deformation and recrystallization behavior of the commercial magnesium alloys. WE54 was analyzed using the strain rates 0.01, 0.1, 1, and 5 s^{-1} in the temperature range from 400 to 550 °C. They concluded that the extent of recrystallization and the localization of the nucleation varied, significantly depending on the temperature and strain rate. At the low temperature recrystallization was very limited and observed at grain boundaries, shear bands, and twin boundaries. Increasing temperatures result in an increased recrystallized fraction, while lower strain rates promote grain-boundary nucleation and reduce shear banding and twinning.

According to the DMM model, the workpiece is considered as a power dissipater in two complementary ways: (1) the power dissipated by plastic work (G) is called the content; and (2) the power dissipated by metallurgical processes (J) is called the co-content. Quan et al. [20] built processing maps for the 42CrMo high-strength steel, and showed that these metallurgical processes can include dynamic recovery, dynamic recrystallization, internal fracture, dissolution or growth of particles, deformation-induced phase transformation, and dynamic precipitation. Liu et al. [21] in their study on processing maps of a Ni-base superalloy concluded that when these metallurgical processes occur, they dissipate power; hence, they contribute to the change in the dissipated power co-content.

The instantaneous flow stress (σ) of the workpiece under hot deformation, at a constant temperature and strain rate, may be given by the constitutive equation, $\sigma = C\dot{\varepsilon}^m$, where C is the strength coefficient, $\dot{\varepsilon}$ is the strain rate, and m the strain-rate sensitivity exponent.

The m coefficient determines the relative change of the two dissipation energies (J and G) at any given strain and temperature, as given by

$$m = \frac{\partial J}{\partial G} = \frac{\partial \ln \sigma}{\partial \ln \dot{\varepsilon}}. \tag{1}$$

The strain-rate sensitivity exponent, m, is important because it is a key factor for evaluating the workability by calculating the power dissipation efficiency, η, which represents how efficiently the energy dissipates through metallurgical processes during plastic deformation. It is given by

$$\eta = \frac{2m}{m+1}. \tag{2}$$

The efficiency of power dissipation is a dimensionless parameter and is considered to be an indication of a material's hot workability. The variation of η with temperature and strain rate constitutes the processing map, which is divided into regions that are correlated with the various microstructural mechanisms. Conditions that provide the highest η are the most favorable for processing, since they lie in the safe region.

Processing maps need one additional parameter to be useful for metal forming processes, which is the instability coefficient (ξ), which helps to delineate regions where unstable flow, fractures, or defects are most likely to occur. The variation of the instability parameter as a function of temperature and strain rate represents an instability map that is obtained by using the principle of maximum entropy rate production, and is given by

$$\xi = \frac{\partial \ln\left[\frac{m}{1+m}\right]}{\partial \ln \dot{\varepsilon}} + m < 0. \tag{3}$$

A microstructural instability is likely in regions where Eq. (3) is satisfied (namely, $\xi < 0$), so the appropriate processing conditions are determined by superimposing both the efficiency of power dissipation

map (η) and the instability map (ξ) to construct a useful processing map.

The method proposed by Prasad et al. [18] for the calculation of these maps has been questioned, since it assumes that the strain-rate sensitivity exponent, m, is a constant. At a given strain, m often varies as a function of strain rate and temperature for complex alloy systems, hence the flow stress does not exactly obey the power law as shown by Murty et al. [22] when they identified flow instabilities in the hot working of the stainless steel AISI 304.

Therefore, if m is not constant, Eq. (2) for η may give erroneous results. For this reason, Murty and Rao [23] proposed a more strict plastic instability criterion where m is a variable, and the η parameter is expressed by

$$\eta = \frac{\frac{m\dot{\varepsilon}^m}{m+1}\big|\dot{\varepsilon}_{\min} + \int_{\dot{\varepsilon}_{\min}}^{\dot{\varepsilon}} m\dot{\varepsilon}^m d\dot{\varepsilon}}{\frac{\dot{\varepsilon}^{m+1}}{2}}. \tag{4}$$

Murty and Rao [23] derived an instability region criterion that is suitable for any stress and strain rate. The revised definitions of J and η are defined by

$$J = \int_0^\sigma \dot{\varepsilon}d\sigma \Rightarrow \frac{\partial J}{\partial \dot{\varepsilon}} = \frac{\dot{\varepsilon}\partial \sigma}{\partial \dot{\varepsilon}} = \frac{\sigma\partial \ln \sigma}{\ln \dot{\varepsilon}} = m\sigma \tag{5}$$

$$\eta = \frac{J}{J_{\max}} = \frac{2J}{(\dot{\varepsilon}\sigma)} \Rightarrow \frac{J}{\dot{\varepsilon}} = \eta\frac{\sigma}{2}. \tag{6}$$

They used a criterion based on the continuum principle, as applied to large plastic flow proposed by Sneddon et al. [24], which was also used by Srinivasan and Prasad [25], for delineating the instability region in processing maps. According to the Murty and Rao criterion, the flow instability occurs when the inequality given by

$$\frac{\partial J}{\partial \dot{\varepsilon}} < \frac{J}{\dot{\varepsilon}} \tag{7}$$

is true.

Relating Eqs. (5) and (6) with Eq. (7), Murty and Rao wrote the instability criterion as

$$\xi(\dot{\varepsilon}) = \frac{2m}{\eta} - 1 < 0. \tag{8}$$

The criterion can be rewritten in the form of an inequality as

$$2m < \eta. \tag{9}$$

Thus, for stable flow, $\eta < 2m$ and $0 < m < 1$.

Ma et al. [26] compared four plastic instability criteria (Prasad, Murty, Gegel, and Malas) based on hot compression tests of Ti-22Al-25Nb alloys. They concluded that Gegel's criterion and Mala's criterion are more effective at high temperatures and low strain rates. However, at high strain rates both criteria are discontinuous. They also found that the instability regions predicted by Prasad's criterion and Murty's criterion are similar, and concluded that both criteria are effective at high strain rates. According to those authors, the advantage of Murty's criterion is that it provides more accurate predictions, due to its theoretical basis and more rigorous calculations; as a result, Murty's criterion can be applied to many σ-$\dot{\varepsilon}$ relationships.

Materials and experiments

The microalloyed steels used in the current study were the hot-rolled DIN 38MnSiVS5 (modified AISI 15V41), and a high-sulfur content steel, designated as 0.39C1.47Mn (AISI 15V41 with high S). Table 1 shows the nominal chemical composition of both steels. The higher sulfur content in these two steels is to enhance the machinability after forging but may cause difficulties during forging.

Figure 1 shows representative micrographs of the longitudinal section of both DIN 38MnSiVS5 and 0.39C1.47Mn steels, in the as-received condition at the mid-radius of the bars. Both alloys exhibited a ferrite–pearlite microstructure (Fig. 1a, b) with MnS inclusions elongated in the rolling direction, as seen in the non-etched images (Fig. 1c, d).

The inclusions in the DIN 38MnSiVS5 steel are more distributed; some of them are globular and smaller, when compared to the inclusions in the 0.39C1.47Mn steel. Optical microscopy examination indicated that the bands of perlite and ferrite are more prominent in the 0.39C1.47Mn steel. Such ferrite and pearlite banding is probably due to the alloy's segregation during the initial solidification, when the alloying elements are rejected into the interdendritic regions and then become prominent after hot rolling as stated by Xu et al. [27] in their investigation of banding and diffusion of phosphorus in steels.

Cylindrical compression samples were machined from hot-rolled bars with the axis of symmetry in the rolling direction. They were extracted from the mid-radius of the bar, and were 10 mm in diameter by 15 mm in height.

To investigate the hot deformation behavior, compression tests were carried out on a Gleeble® 3500 thermomechanical simulator at temperatures ranging from 900 to 1200 °C at intervals of 50 °C, and for strain rates of 0.3, 1.0, 3, 10, and 30 s^{-1} to a targeted true strain of 1.0. The specimens were heated to the deformation temperature at 10 °C/s and held for 60 s before compression. All the specimens were quenched immediately after compression in water in order to preserve the microstructure at the end of each test.

Processing maps were constructed for strains of 0.1–0.9 in increments of 0.1 and for a strain of 0.96 for both steels. Some samples were prepared for light optical

Table 1 Nominal chemical composition of steels DIN 38MnSiVS5 and 0.39C1.47Mn (wt pct)–Fe balance

Steel	C	Mn	P	S	Si	Ni	Cr	Mo	Cu	Al	V
38MnSiVS5	0.37	1.32	0.010	0.064	0.62	0.08	0.13	0.02	0.19	0.020	0.086
0.39C1.47Mn	0.39	1.47	0.012	0.110	0.26	0.06	0.10	0.02	0.14	0.002	0.070
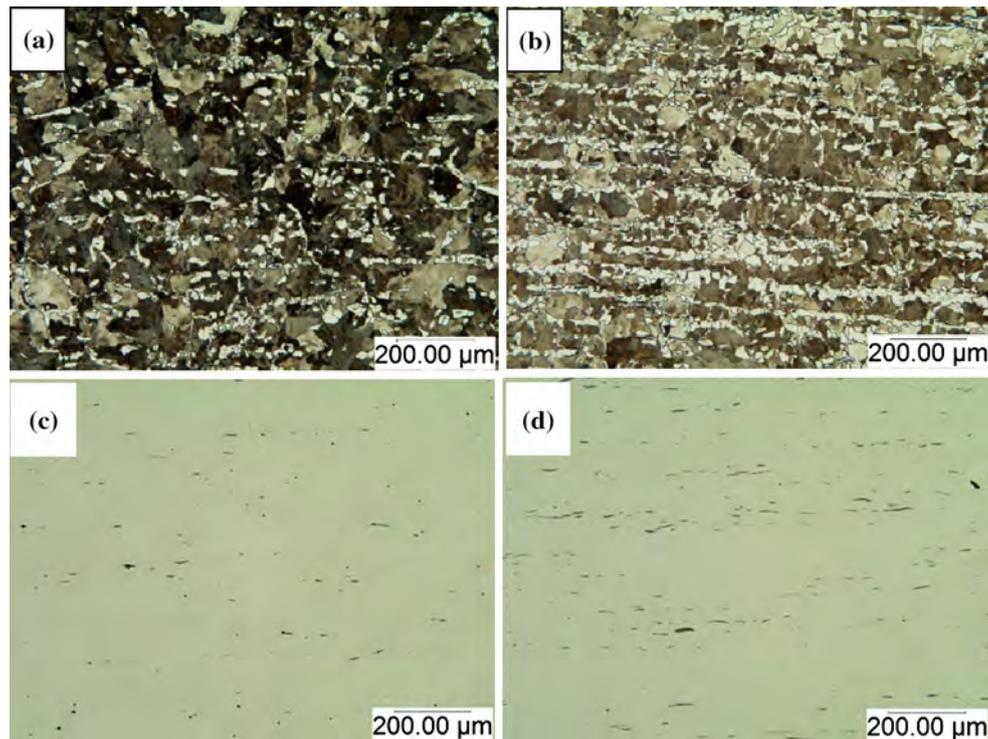
Fig. 1 Representative micrographs of the as-received steels **a** DIN 38MnSiVS5 and **b** 0.39C1.47Mn microalloyed steels from the mid-radius of the bar–light optical micrograph (LOM), 2 % nital solution; and **c** and **d** as polished, respectively, for each steel–LOM

microstructural analysis and other samples were analyzed by scanning electron microscopy (SEM).

Results and discussion

Flow curves

Figures 2 and 3 show the true stress–true strain curves of both DIN 38MnSiVS5 and 0.39C1.47Mn steels obtained from the compression tests in the Gleeble. The flow stress is very sensitive to the deformation temperature and the strain rate: it increases with increasing strain rate at the same temperature and decreases with increasing temperature at the same strain rate.

The curves of both steels exhibit similar characteristics. They increase to a maximum value at a certain strain as a result of strain hardening, followed by a moderate and steady flow (except for the highest strain rates of 10 and 30 s^{-1}). The peak stress is due to rapid multiplication of dislocations with increasing strain.

When the strain reaches a critical value, dynamic softening due to various mechanisms, such as dynamic recrystallization (DRX), occurs and balances the strain hardening effect, which leads to the final constant flow stress (i.e., steady flow). It can be seen at the highest strain rates of 10 and 30 s^{-1} that strain hardening dominates at strains up to 0.3 followed by a steady decrease in flow stress with further strain. At these strain rates, a balance between strain hardening and softening is not attained, and as a result, a steady flow stress is not observed. The dynamic recrystallization proceeds slowly at a low deformation temperature and a high strain rate. The low temperature provides limited energy for grain boundary mobility, and the high strain rate does not provide enough time for the nucleation and growth of dynamically recrystallized grains as also observed in the work of Lin et al. [28].

The work of Sun et al. [29] and Jorge-Badiola and Gutierrez [30] have shown that strain path and especially strain reversal can have an effect on the recrystallization process. The present work has used a single deformation

Fig. 2 Flow curves of DIN 38MnSiVS5 for the strain rates of 0.3 (**a**), 1 (**b**), 3 (**c**), 10 (**d**), and 30 s^{-1} (**e**) at deformation temperatures of 900, 950, 1000, 1050, 1100, 1150, and 1200 °C
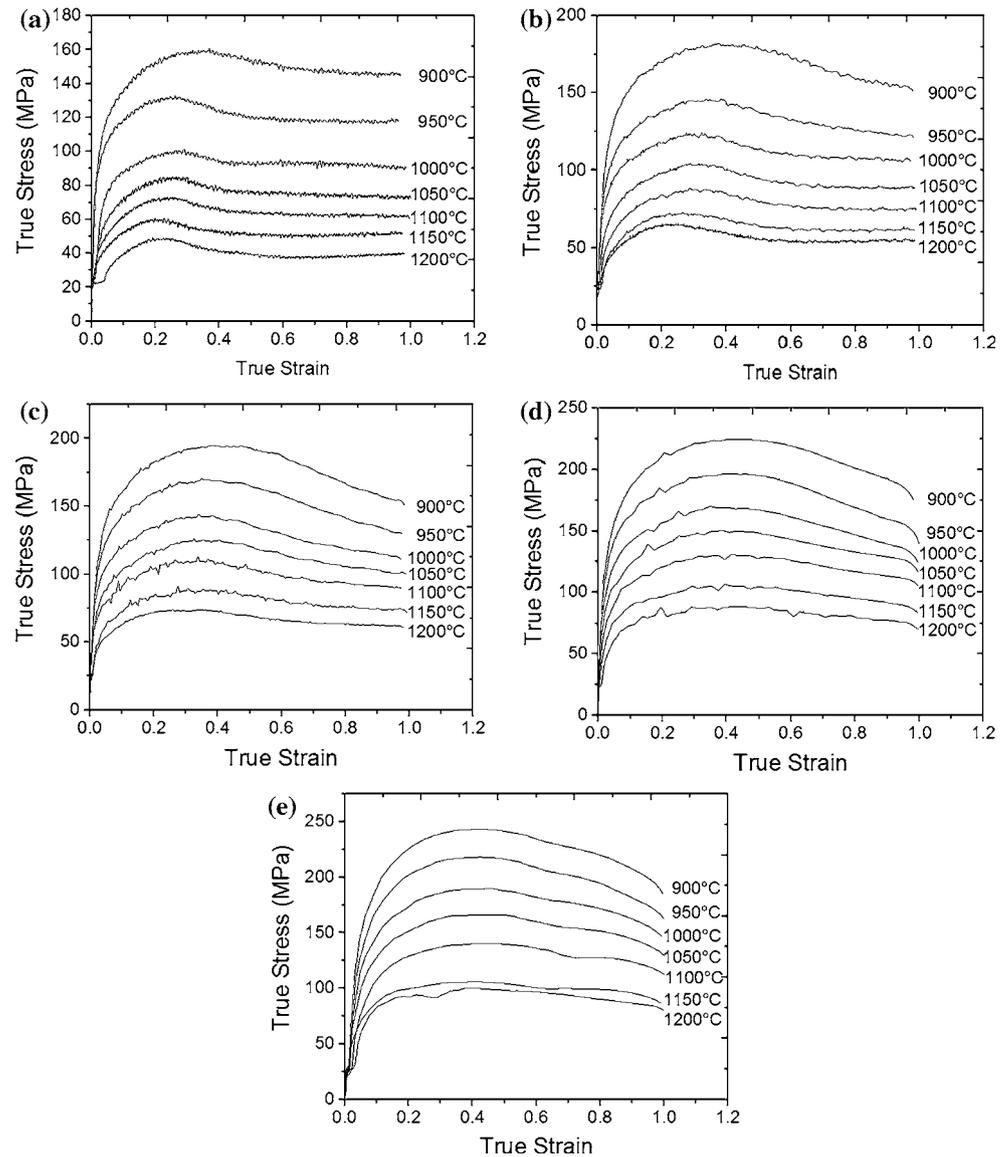
path and if a very complex forging is to be produced from these steels then the effect of strain path changes would need to be evaluated. Unfortunately, such an evaluation is beyond the scope of the present study.

Strain-rate sensitivity

Strain-rate sensitivity as a function of strain and temperature

The strain-rate sensitivity of the flow stress is the most important parameter in calculating the power dissipation efficiency, and hence, in evaluating the hot workability of the steels. To evaluate the strain-rate sensitivity as a function of strain rate and temperature, m values were calculated for both steels at a compressive strain of 0.96

using Eq. (1), and the results are shown in Tables 2 and 3.

Generally, m varies with the processing conditions. This variation indicates that flow stress does not adhere to the power-law behavior. It can be seen that there are negative m values at 1150 °C and at high strain rates. Negative strain-rate sensitivity can occur under conditions that promote flow instability, such as dynamic strain aging (DSA), adiabatic shear band (ASB) formation, or the initiation and growth of micro-cracks, as observed in the work of Quan et al. [20].

Strain-rate sensitivity as a function of temperature

Another way to obtain the strain-rate sensitivity is through the constitutive equation, which effectively describes the correlation between flow stress, strain rate, and deformation

Fig. 3 Flow curves of 0.39C1.47Mn for the strain rates of 0.3 (**a**), 1 (**b**), 3 (**c**), 10 (**d**), and 30 s^{-1} (**e**) at deformation temperatures of 900, 950, 1000, 1050, 1100, 1150, and 1200 °C
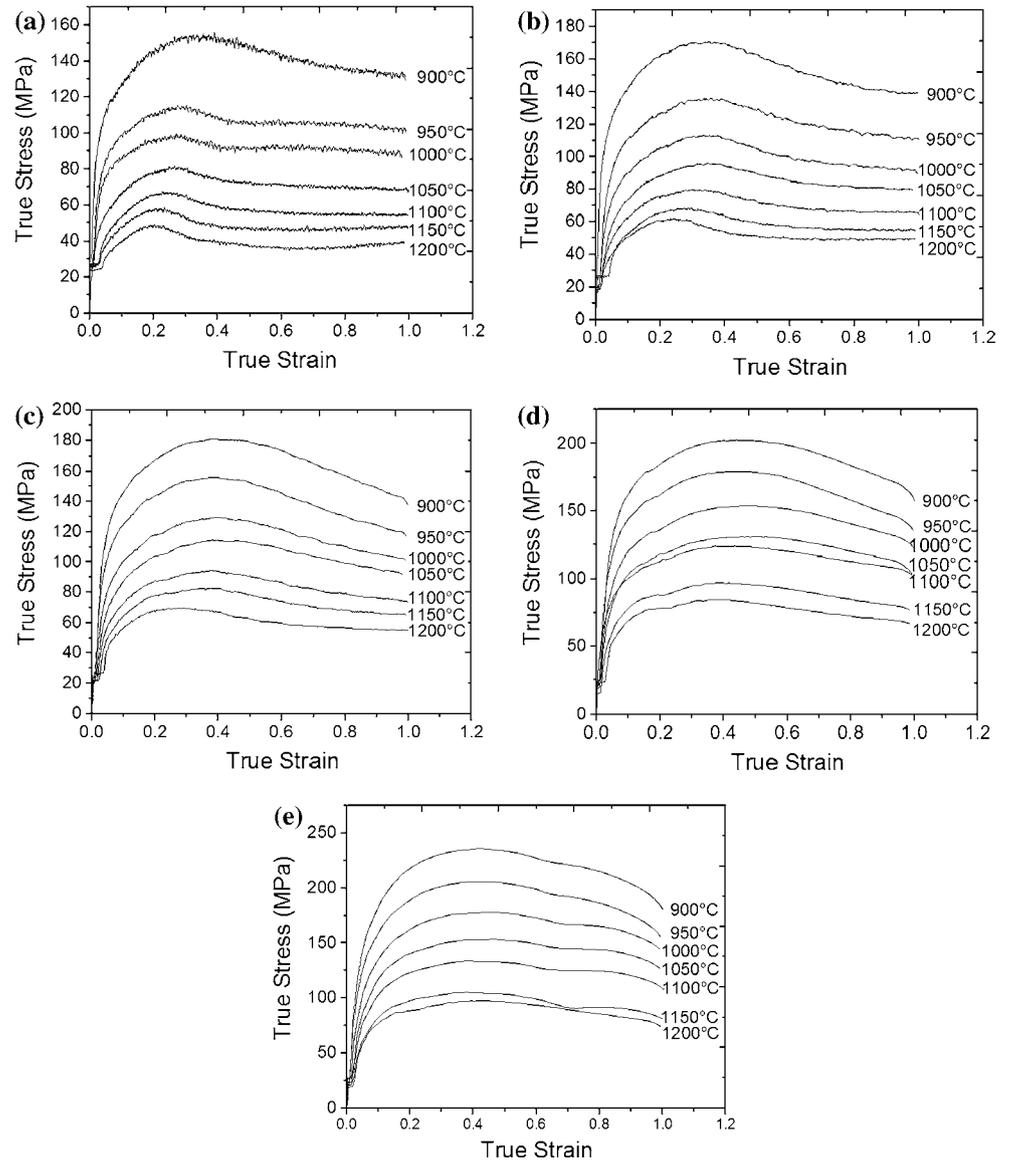
Table 2 *m* values calculated at different temperatures and strain rates for DIN 38MnSiVS5

True strain	Strain rate (s^{-1})	Temperature (°C)						
		900	950	1000	1050	1100	1150	1200
−0.96	0.3	0.051	0.034	0.142	0.160	0.165	0.156	0.278
	1	0.026	0.047	0.092	0.134	0.168	0.156	0.188
	3	0.074	0.102	0.095	0.147	0.168	0.150	0.134
	10	0.107	0.116	0.135	0.131	0.116	0.052	0.172
	30	0.068	0.087	0.123	0.076	0.065	−0.039	0.176

temperature. The strain-rate sensitivity can be calculated using different expressions, such as an exponential relationship, a power exponent relationship, or a hyperbolic sine, given the three Eqs. (10), (11), and (12) based on the Arrhenius equation for the temperature dependence.

$$\dot{\varepsilon} = A_1 \sigma^{n_1} \exp(-Q/RT) \qquad (10)$$

$$\dot{\varepsilon} = A_2 \exp(\beta\sigma) \exp(-Q/RT) \qquad (11)$$

Table 3 m values calculated at different temperatures and strain rates for 0.39C1.47Mn

True strain	Strain rate (s^{-1})	Temperature (°C)						
		900	950	1000	1050	1100	1150	1200
−0.96	0.3	0.027	0.052	0.028	0.107	0.13	0.087	0.164
	1	0.036	0.074	0.067	0.146	0.156	0.144	0.172
	3	0.075	0.109	0.145	0.147	0.205	0.174	0.139
	10	0.142	0.149	0.185	0.164	0.219	0.098	0.2
	30	0.167	0.161	0.191	0.219	0.101	−0.017	0.258

$$\dot{\varepsilon} = A[\sinh(\alpha\sigma)]^n \exp(-Q/RT), \tag{12}$$

where $\dot{\varepsilon}$ is the strain rate (s^{-1}), σ is the flow stress (in MPa), n is the stress exponent, Q is the deformation activated energy (kJ mol^{-1}), T is the temperature (K), R is the gas constant (8.31 $mol^{-1}K^{-1}$); A, A_1, A_2, n_1, β, and α are the material constants, and $\alpha = \beta/n_1$.

Taking the natural logarithm of both sides of Eqs. (10), (11), and (12), respectively, the following can be obtained:

$$\ln\dot{\varepsilon} = \ln A_1 + n_1 \ln\sigma - (Q/RT) \tag{13}$$

$$\ln\dot{\varepsilon} = \ln A_2 + \beta\sigma - (Q/RT) \tag{14}$$

$$\ln\dot{\varepsilon} = \ln A + n\ln[\sinh(\alpha\sigma)] - (Q/RT). \tag{15}$$

Since $n_1 = \partial\ln\dot{\varepsilon}/\partial\ln\sigma$, and $\beta = \partial\ln\dot{\varepsilon}/\partial\sigma$, n_1 and β can be evaluated from the slopes of parallel lines from different temperatures in a plot of $\ln\dot{\varepsilon}$ versus $\ln\sigma$, and $\ln\dot{\varepsilon}$ versus σ, respectively. Figures 4 and 5 show the data from the true–true strain curves examined by Eqs. (13) and (14). Figures 4 and 5 were used to calculate the parameter α, and consequently the m values, in a steady flow stress at a strain of 0.96.

From Eq. (15), the stress exponent n can be obtained from the slope of $\ln\dot{\varepsilon}$–$\ln[\sinh(\alpha\sigma_{ss})]$ curve. Figure 6 shows these curves. The strain-rate sensitivity exponent $m = 1/n$ can be calculated as a function of the temperature.

The strain-rate sensitivity has a strong effect on the energy absorption capability of the material, which is larger when m is positive and when strain hardening is significant. In this situation, the material tends to support the deformation by increasing the absorption of energy before failure as concluded by Ozturk et al. [31].

Figure 7 shows the variation of m as a function of temperature, obtained by Eqs. (10) to (15). It can be seen that m is positive and increases with increasing temperature for almost all temperatures, except between 1100 and 1150 °C, where the strain-rate sensitivity drops.

In order to compare m as a function of temperature and strain rate [$m = f(T, \dot{\varepsilon})$], and also only as a function of temperature [$m = f(T)$], m curves were also plotted for both microalloyed steels for the lower and higher strain rate using the data from Tables 2 and 3. Figure 8 shows these plots.

It can be observed that m is not constant as a function of strain rate. At the lower strain rate, m values of DIN 38MnSiVS5 are more stable than for 0.39C1.47Mn. From 1000 °C to 1150 °C, m drops for both steels and becomes negative at the strain rate of 30 s^{-1}, which indicates some type of plastic instability. Comparing $m = f(T)$ and $m = f(T, \dot{\varepsilon})$, it can be seen that despite the different results, they do show a coherent behavior, which is confirmed by the drop at 1150 °C in both situations. In addition, while m is higher at 1200 °C in both cases, a positive m value does not necessarily represent a safe region.
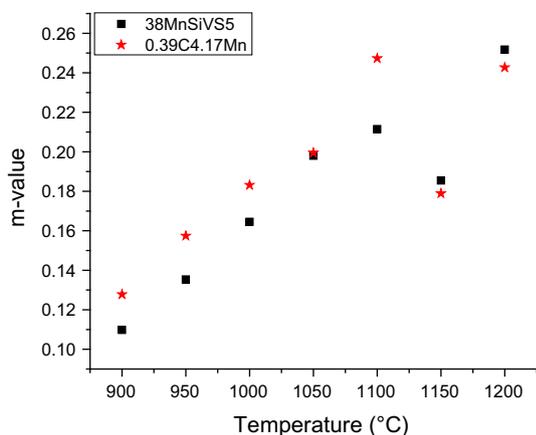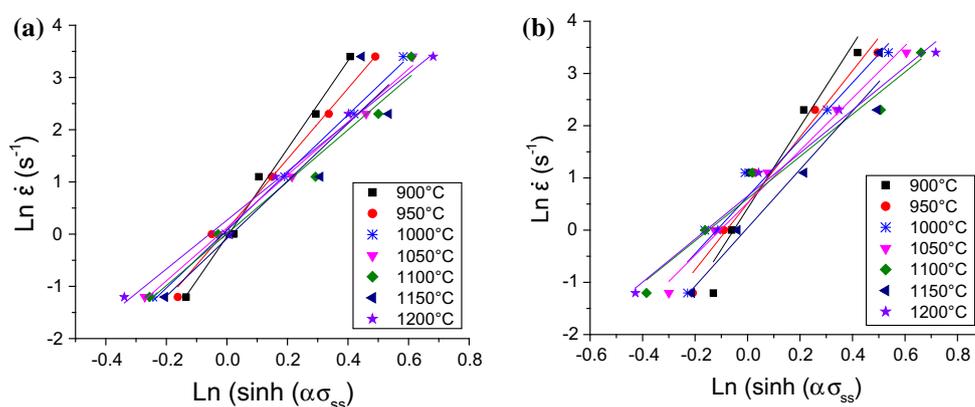
Fig. 4 The relationship between $\ln\dot{\varepsilon}$ versus $\ln\sigma_{ss}$ for **a** DIN 38MnSiVS5, and **b** 0.39C1.47Mn microalloyed steels
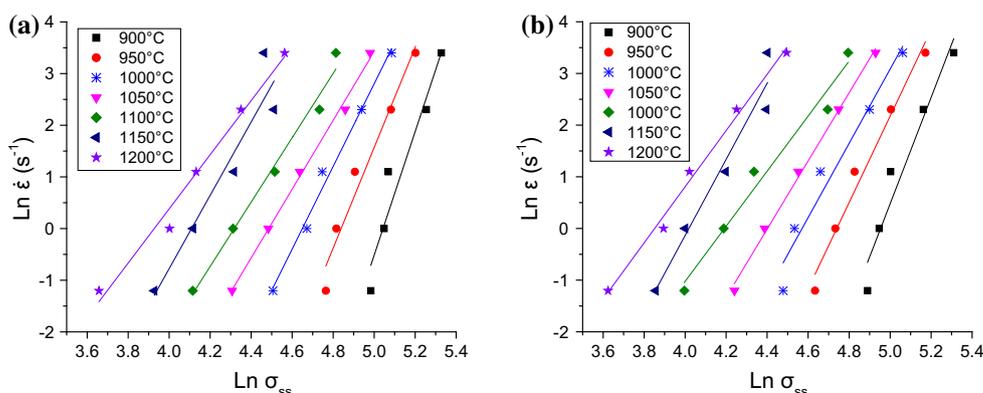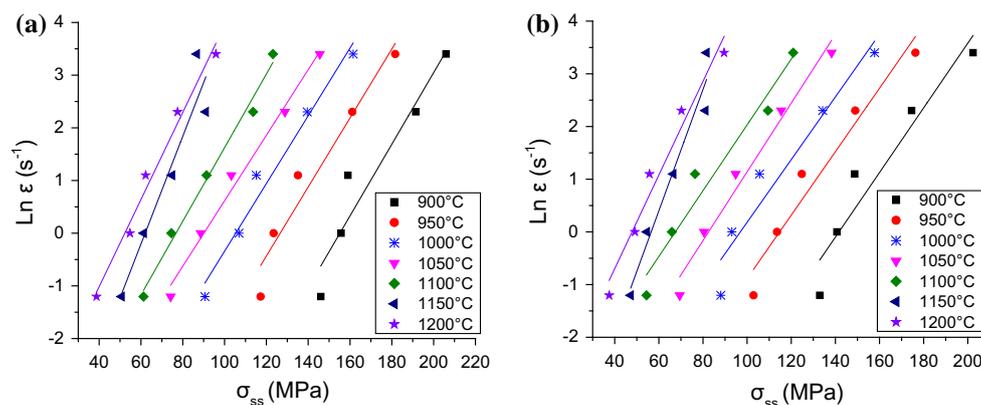
Fig. 5 The relationship between and $\ln \dot{\varepsilon}$ versus σ_{ss} for **a** DIN 38MnSiVS5, and **b** 0.39C1.47Mn microalloyed steels

Fig. 6 The relationship between $\ln \dot{\varepsilon}$ versus $\ln[\sinh(\alpha\sigma_{ss})]$ for **a** DIN 38MnSiVS5, and **b** 0.39C1.47Mn microalloyed steels

Fig. 7 Strain-rate sensitivity as a function of only temperature

Power dissipation efficiency maps

The m values presented in Tables 2 and 3 were used to calculate the efficiency of power dissipation, η, so efficiency maps could be constructed for both steels.

In Prasad's criterion, m is constant, and cannot be used, since the current study has demonstrated that m varies with the processing conditions. For this reason, Murty's criterion was used instead of Prasad's. Figure 9 shows the power dissipation efficiency maps for a compressive strain of 0.96 for the two steels. Each iso-efficiency contour represents a dynamic microstructural state of the material, and may be seen as a microstructure path. The power dissipation maps of DIN 38MnSiVS5 and 0.39C1.47Mn show differences that are probably due to different chemical compositions.

The map for DIN 38MnSiVS5 shows η ranging from about 0.10–0.32. The highest efficiencies are between 1150 and 1200 °C for strain rates of 0.3 to 1 s^{-1}, while the lowest are at 1150 °C for strain rates of 10–30 s^{-1}.

For 0.39C1.47Mn η varies in the range of about 0.09–0.39. The peak efficiency of 0.39 is at the highest strain rate at 1100 °C. Both maps exhibit low efficiency at lower temperatures and lower strain rates.

Regions with high power dissipation efficiency are not necessarily safe regions, so instability maps must also be generated and evaluated.
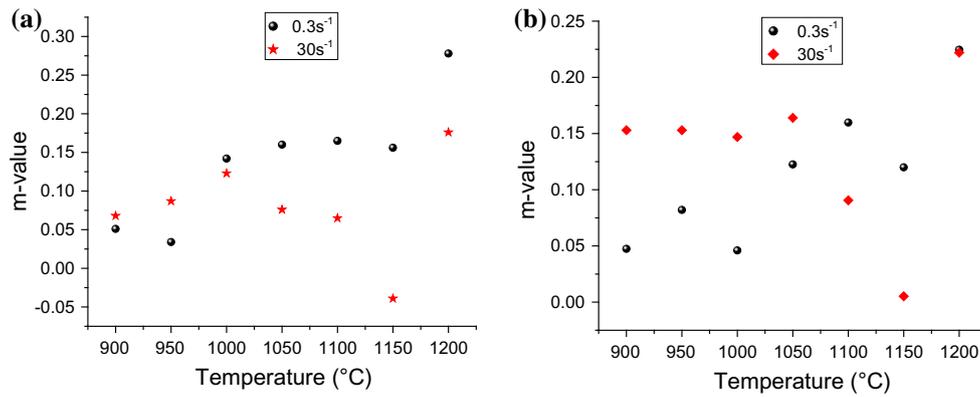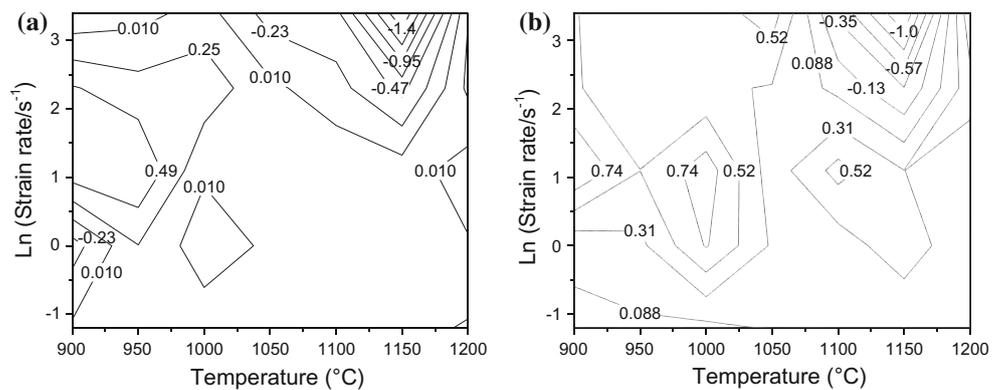
Fig. 8 Strain-rate sensitivity as a function of both temperature and strain rate for **a** DIN 38MnSiVS5 and **b** 0.39C1.47Mn

Fig. 9 Power dissipation maps at true compressive strain 0.96 for **a** DIN 38MnSiVS5 and **b** 0.39C1.47Mn, based on Murty's criterion
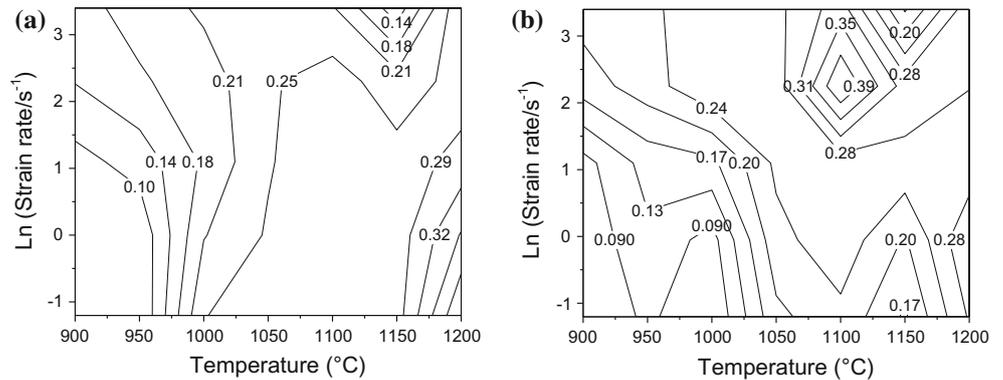
Fig. 10 Instability maps at true compressive strain 0.96 for **a** DIN 38MnSiVS5 and **b** 0.39C1.47Mn, based on Murty's criterion

Instability maps

Figure 10 shows the variation of the instability parameter, ξ, at a compressive strain of 0.96 for different temperatures and strain rates for both DIN 38MnSiVS5 and 0.39C1.47Mn steels. Unsafe regions are the areas with negative ξ values. In both maps, the flow instability region is limited to a single area. For 38MnSiVS5, the contours for ξ are as low as −1.4, while for 0.39C1.47Mn, the lowest contour is at −1.0.

The response of strain-rate sensitivity to strain, temperature, and strain rate is responsible not only for the variation of power dissipation efficiency, but also for the variation of instability. Consequently, regions with low m values correspond to unstable areas. The m values for both steels in the current study are negative at the temperature of 1150 °C and strain rate of 30 s^{-1}. However, high values of strain-rate sensitivity do not necessarily represent a safe area due to the complexity in the dynamic transition or the coexistence of different deformation

mechanisms induced by the combination of processing parameters [20].

Hence, the safe and unsafe domains in the processing maps must be identified, based on a comprehensive comparison of strain-rate sensitivity, power dissipation efficiency, the instability criterion, and the microstructure of the materials being evaluated.

Processing maps

Processing maps are the result of superimposition of the instability map on the power dissipation efficiency map. By overlapping the two maps, it is possible to determine domains where individual processes occur and the limiting conditions for regimes of flow instability. The contours on processing maps represent the efficiency of power dissipation and shaded regions correspond to flow instability where ξ values are negative. Figure 11 shows the processing maps obtained at a compressive strain of 0.96 for DIN 38MnSiVS5 and 39C1.4Mn steels.

A processing map describes the conditions for microstructural evolution mechanisms and flow instability regions under various processing conditions. The safe regions in the processing map may have the characteristics of complete dynamic recrystallization (DRX) or dynamic recovery (DRV).

The processing maps provide appropriate temperature and strain rate ranges where instabilities should not occur. The shaded regions, which suggest the possibility of an unstable flow, are localized in the current study to high deformation temperatures and high strain rates for two steels. However, to determine the actual cause of the instability, microstructural assessment needs to be conducted after deformation in the regions of temperature and strain rate where instabilities are indicated on the processing maps.

Figure 12 shows the microstructures of the deformed specimens at the temperature of 900 °C and strain rate of 30 s^{-1} for both microalloyed steels. The whole

microstructure is constituted of equiaxed grains, which reveals that softening was dominated by DRX, and therefore, that these regions can be considered safe. The recrystallized fine grain size shows that at high strain rates and low temperatures, smaller recrystallized grains can be easily obtained.

Figure 13 shows signs of secondary DRX with some abnormal grain growth in the microstructure of 38MnSiVS5 specimen compressed at 900 °C and 0.3 s^{-1}, and (b) the 0.39C1.47Mn specimen compressed at 900 °C and 1 s^{-1}. The results are consistent with the processing maps, which reveal a low efficiency of power dissipation, plastic instability can occur through abnormal grain growth, and therefore such processing conditions should be avoided.

During some forming processes, deformable MnS inclusions become elongated and aligned with the material flow as observed by Cyril et al. [32], or remain round, depending on the amount of sulfur, shape control additions during steelmaking, and the processing conditions. In general, the inclusion morphology is controlled by its composition, as well as how and when it is formed.

The morphology of the inclusions remains unchanged after deformation, as compared to the as-received steel; however, the inclusions are more aligned with the material flow. The presence of inclusions in microalloyed steels has a significant effect since they disturb the flow of the metal during deformation, influence the redistribution of structural defects, and significantly affect the movement of dislocations as stated by Lunev and Pirozhkova [33].

The deterioration in the formability properties caused by MnS and other inclusions depends on some characteristics such as size, shape, volume fraction, and distribution. The shape, for example, can give rise to local stress concentrations. When the inclusions are located along grain boundaries in the form of films or chains, they can facilitate crack formation, as shown by Shevtsova et al. [34] who studied the effect of sulfide inclusions on the quality of low-alloy structural steels.

Fig. 11 Processing maps at compressive true strain 0.96 for **a** DIN 38MnSiVS5 and **b** 0.39C1.47Mn, based on Murty's criterion
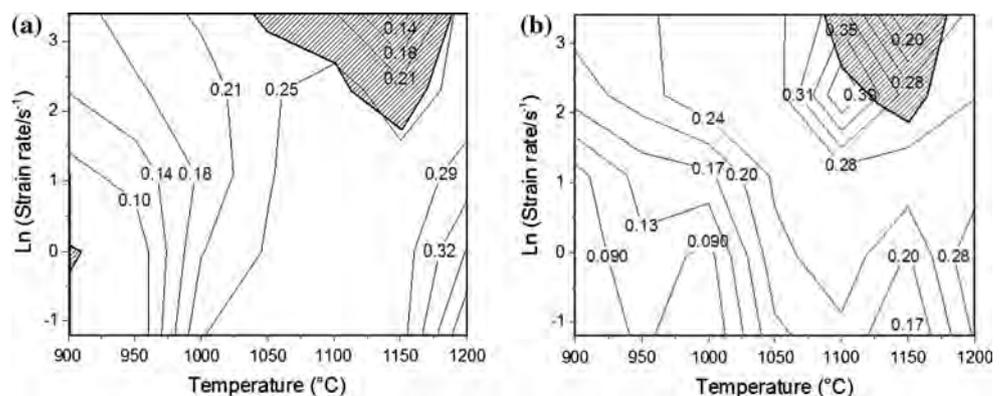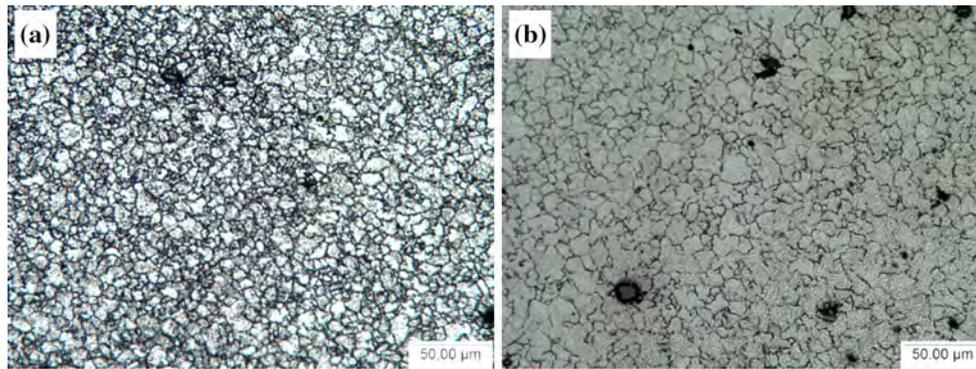
Fig. 12 Representative micrographs of specimens compressed at 900 °C and 30 s^{-1} **a** DIN 38MnSiVS5, and **b** 0.39C1.47Mn, LOM, 2 % nital

Fig. 13 Representative micrographs of **a** DIN 38MnSiVS5 specimen compressed at 900 °C and 0.3 s^{-1}, and **b** 0.39C1.47Mn specimens compressed at 900 °C and 1 s^{-1}, LOM, 2 % nital
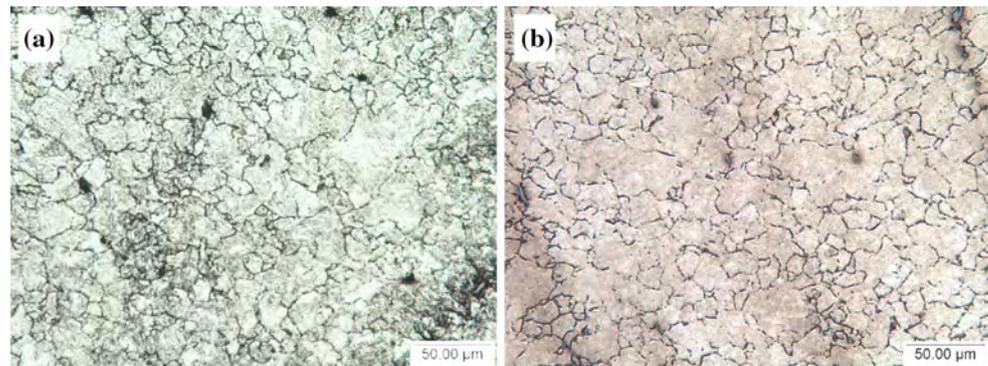

Figure 14 shows a crack in the sample of 0.39C1.47Mn steel deformed at 1150 °C and 30 s^{-1}, which is in the unsafe region. Ma et al. [35] also observed similar cracks in their study on the influence of inclusion on the fatigue of a low carbon steel, and concluded that the stresses in the metal near a crack can produce the conditions necessary for new cracks to form and further discontinuities in the metal to occur.

Figure 15 shows a highly magnified image of the central region of the DIN 38MnSiVS5 steel. The large void was probably caused by a MnS inclusion, and voids in the steel might be a cause of instability. Despite the compressive stress ability to close voids, the voids can experience different types of deformation as a result of material flow during compression. Luo [36] in his study on the evolution of voids under hot deformation stated that the presence of inclusions can lead to local inhomogeneous flow, due to the discontinuity at the inclusion–matrix interface. Ma et al. [26] concluded that when inclusions are harder than the surrounding matrix, stresses and strain tend to concentrate around them during matrix deformation and cause matrix–inclusion decohesion or the fracture of hard inclusions, which can result in the formation of voids. Voids in the center of a sample are more harmful, since they can be exposed to different stress states that may facilitate their growth.

The processing maps for both steels show a region of instability at temperatures between 1100 and 1150 °C and at the highest strain rates. For these microalloyed steels (especially the one with the higher sulfur content), care must be taken when forging in temperatures about 1100 °C or higher. High strain rates should be avoided, so it is preferable to forge these steels in a mechanical or hydraulic press rather than in a hammer.

Effect of true strain on processing maps evolution

Figures 16 and 17 show the processing maps for the DIN 38MnSiVS5 and 0.39C1.47Mn steels constructed at the strain range of 0.1–0.96, in increments of 0.1 strain. In general, the processing maps for different true strains exhibit different features indicating that the efficiency of power dissipation and instability change significantly with increasing strain, as seen in these figures. The shaded regions are larger for 38MnSiVS5 than for 0.39C1.47Mn steel at high strain rates, and at temperatures up to a strain of 0.8.

To demonstrate that these processing maps are useful to design hot working processes, ring-shaped specimens (outside diameter 18 mm, inside diameter 9 mm, and thickness 6 mm) were upset at temperatures around 1100 °C, strain rate of 10 s^{-1} to a strain of 0.4. The
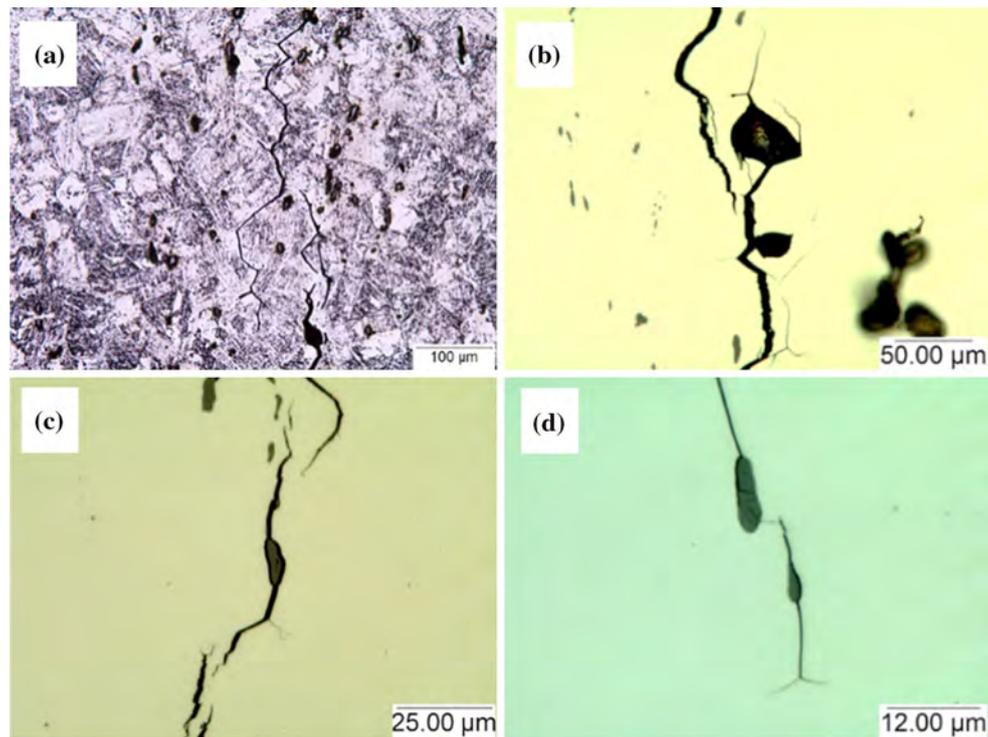
Fig. 14 Representative micrographs of 0.39C1.47Mn steel compressed at 1150 °C and 30 s^{-1}: **a** sample etched with saturated picric acid solution; **b–d** sample with the surface only polished–LOM
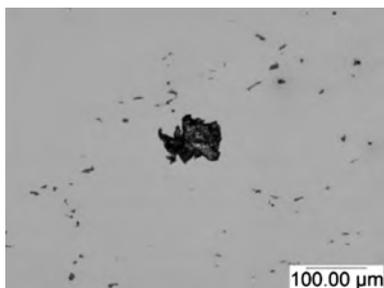
Fig. 15 Representative micrograph of DIN 38MnSiVS5 steel compressed at 1050 °C and 30 s^{-1}, only polished, LOM

corresponding processing map is presented in Fig. 16. Table 4 shows that the specimens were made from a microalloyed steel with a chemical composition that is very close to the DIN 38MnSiVS5 steel that was used to build the processing maps.

Figure 18 shows micrographs of the upset ring specimens: (a) shows a crack, and (b) reveals a crack formation along an inclusion. It can be concluded that the influence of inclusions is more significant at high strain rates and high temperatures that can favor crack formation and propagation, due to stress concentration.

The deformed samples exhibited intergranular fracture, which confirms that for a strain of 0.4 the temperature and strain rate are in an unsafe region in the processing map

(Fig. 16). Figure 19 shows scanning electron microscopy (SEM) images of the crack surface in the deformed sample. Figure 19b shows that elongated sulfides were found on the fracture surface, and were confirmed by energy dispersive spectrometry (EDS).

Conclusions

The present study constructs processing maps for the evaluation of hot workability of 0.39C1.47Mn and DIN 38MnSiVS5 microalloyed steels from isothermal compression test data. Hot compression tests were carried out in the range of 900–1200 °C and at strain rates of 0.3, 1, 3, 10, and 30 s^{-1}. The isothermal compression data were analyzed to construct processing maps, which indicate the safe and unsafe processing regions.

The *m* values were estimated from data acquired in the thermomechanical tests and were used to calculate the efficiency of power dissipation map and the instability map. Processing maps were constructed from the overlap of both the maps. The constitutive behavior of both steels under hot working conditions was defined and the unsafe regions were identified.

The processing maps for both steels show a region of instability at temperatures between 1100 and 1150 °C and
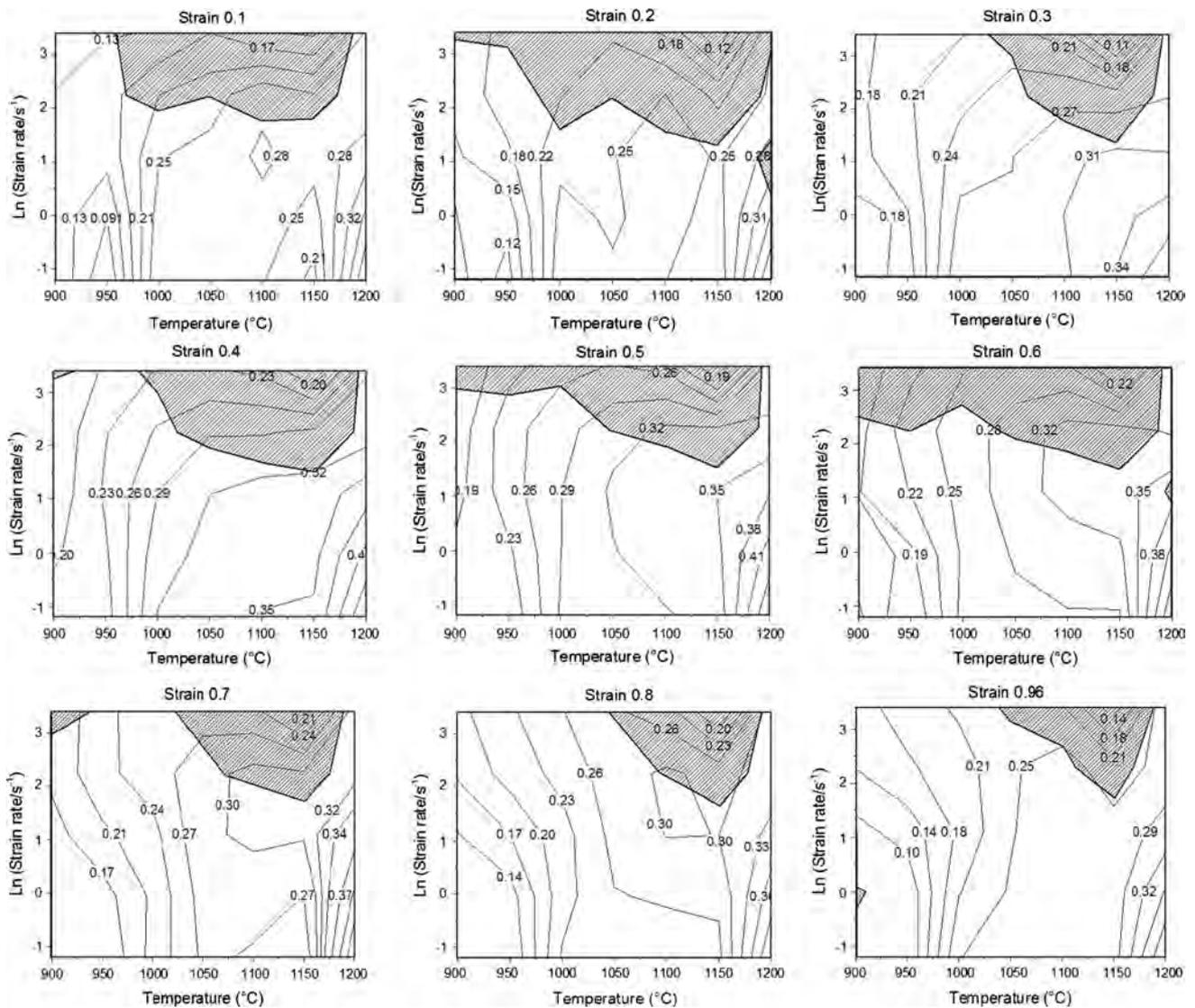
Fig. 16 Processing maps of DIN 38MnSiVS5 steel under the true compressive strain of 0.1–0.96

at high strain rates (namely, those from 10.0 to 30.0 s^{-1}). Metallographic analysis was performed on samples deformed under these unstable conditions. Cracks were found in the 39C1.47Mn steel samples around sulfides, and were probably the cause of the flow instability.

Dynamic recrystallization was the main power dissipation mechanism that occurred in the safe regions. However,

regions of low power dissipation efficiency can undergo abnormal grain growth, so they should be avoided.

The influence of inclusions is more significant at high strain rates and high temperatures, where they can favor crack formation and propagation, due to stress concentration. For these microalloyed steels, especially with a high sulfur content, care must be taken when forging at temperatures near
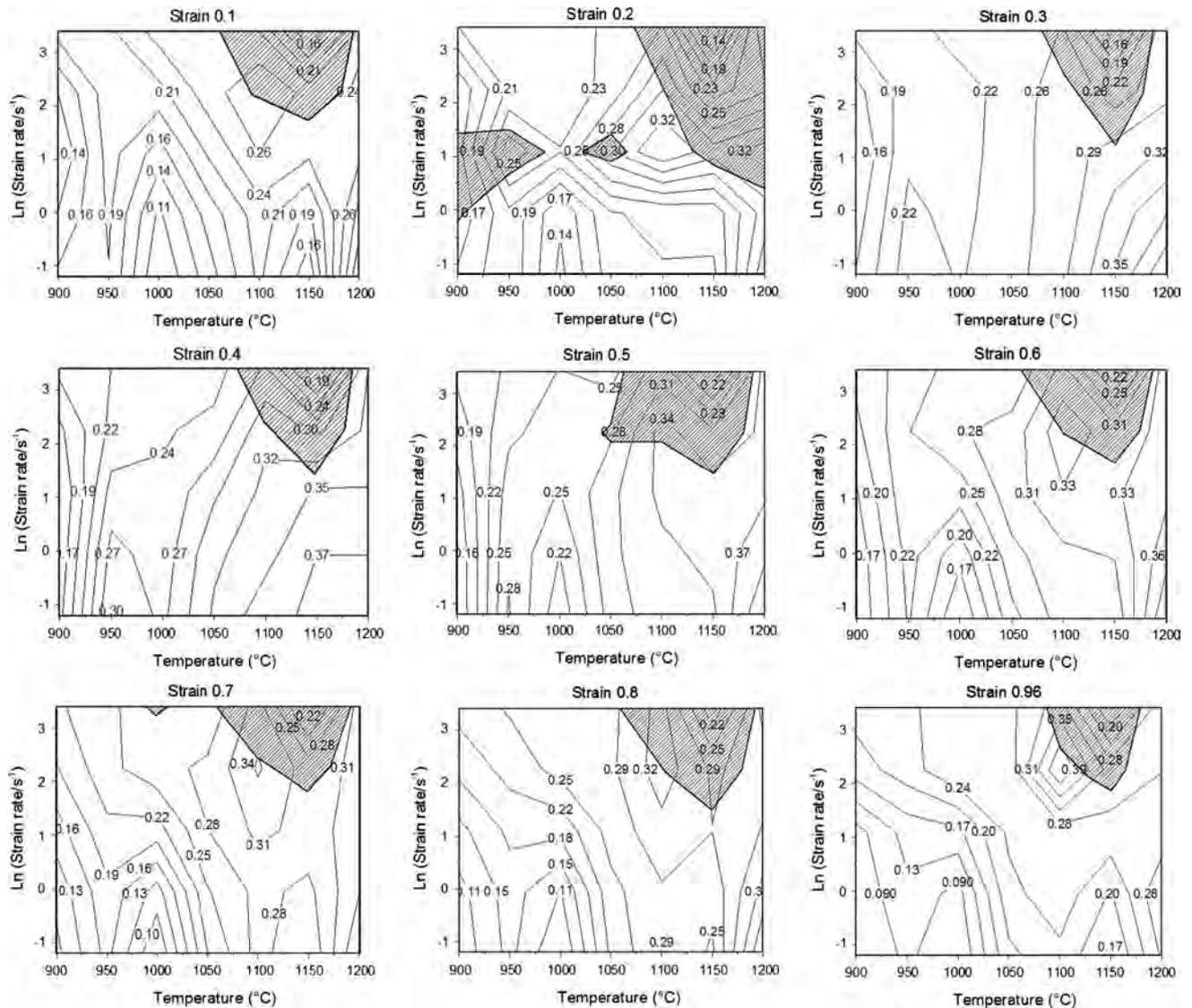
Fig. 17 Processing maps of 0.39C1.47Mn steel under the true compressive strain of 0.1–0.96

Table 4 Nominal chemical composition of steels DIN 38MnSiVS5 (wt pct)—Fe balance

Steel	C	Mn	P	S	Si	Ni	Cr	Mo	Cu	Al	V
38MnSiVS5	0.37	1.41	0.014	0.055	0.6	0.10	0.11	0.02	0.04	0.011	0.09

1100 °C. Since higher strain rates should be avoided, it may be preferable to forge these steels in slower speed presses rather than in high-speed forging hammers.

The processing map of DIN 38MnSiVS5 microalloyed steel was evaluated with a hot ring compression test. The results showed that the processing map is consistent, and

Fig. 18 Representative micrograph of DIN 38MnSiVS5 steel compressed at 1100 °C, 10 s^{-1} and strain 0.4: **a** 2 % nital; and **b** polished, LOM
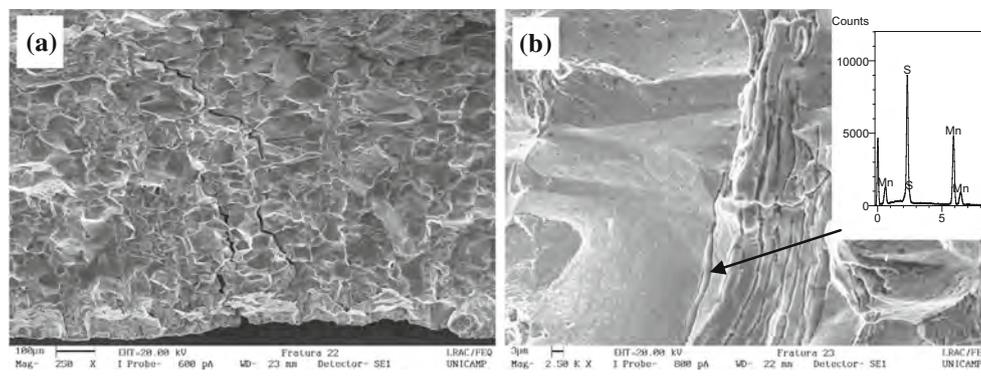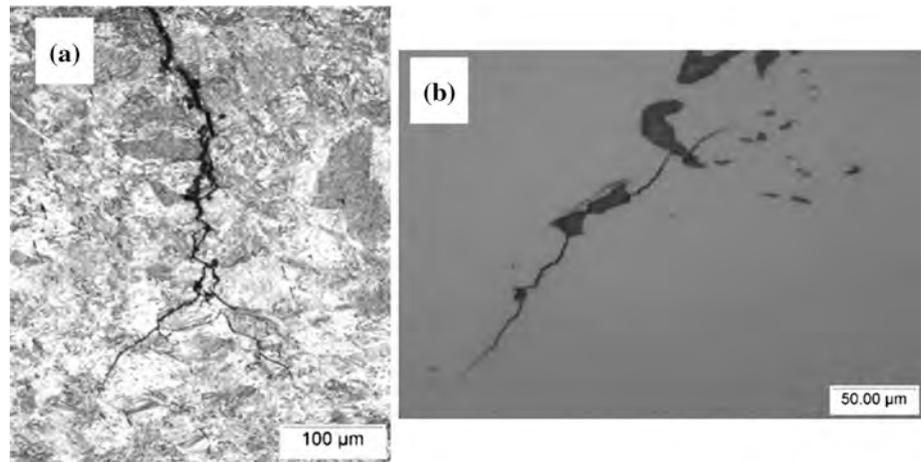
Fig. 19 SEM images of the sample deformed at a temperature of 1100 °C, 10 s^{-1} and strain 0.4: **a** crack surface and **b** EDS of one elongated sulfide

can be useful for the safe hot working of the studied microalloyed steel.

Compliance with ethical standards

Conflict of interest Authors do not identify any potential conflicts of interest related to this work.

Ethical approval This research did not involve human participants or animals. No figures, tables, or text passages already published elsewhere were included in this work, therefore no consent or permission was necessary.

References

1. Bu FZ, Wang XM, Chen L, Yang SW, Shang CJ, Misra RDK (2015) Influence of cooling rate on the precipitation behavior in Ti–Nb–Mo microalloyed steels during continuous cooling and relationship to strength. Mater Charact 102:146–155. doi:10.1016/jmatchar201503005

2. Zhang X, Cai Q, Zhou G, Chen Q, Xiong Y (2011) Microstructure and mechanical properties of V-Ti–N microalloyed steel used for fracture splitting connecting rod. J Mater Sci 6:1789–1795. doi:10.1007/s10853-010-5002-6

3. Kim KW, Park JK (2015) A study of the dynamic recrystallization kinetics of V-microalloyed medium carbon steel. J Mater Sci 18:641–6153. doi:10.1016/s10853-015-9171-1

4. Hajisafari M, Nategh S, Yoozbashizadeh H, Ekrami A (2013) Improvement in mechanical properties of microalloyed steel 30MSV6 by a precipitation hardening process. J Iron Steel Res Int 20:66–73. doi:10.1016/S1006-706X(13)60100-4

5. Mejía I, Altamirano G, Bedolla-Jacuinde A, Cabrera JM (2014) Modeling of the hot flow behavior of advanced ultra-high strength steels (A-UHSS) microalloyed with boron. Mater Sci Eng A 610:116–125. doi:10.1016/jmsea201404105

6. Wei H, Liu G, Zhao H, Zhang M (2014) Effect of carbon content on hot deformation behaviors of vanadium microalloyed steels. Mater Sci & Eng A 596:112–120. doi:10.1016/jmsea201312063

7. Prasad YVRK, Sasidhara S (1997) Hot working guide: a compendium of processing maps. ASM International, Materials Park

8. Omar AA, Cabrera JM, Prado JM (1996) Characterization of the hot deformation in a microalloyed medium carbon steel using processing maps. Scr Mater 34:1303–1308. doi:10.1016/1359-6462(95)00651-6

9. Gu S, Zhang L, Ruan J, Zhou P, Zhen Y (2014) Constitutive modeling of dynamic recrystallization behavior and processing map of 38MnVS6 non-quenched steel. J Mater Eng Perform 23:1062–1068. doi:10.1007/s11665-013-0808-4

10. El Hassani FB, Chenaoui A, Dkiouak R, Elbakkali L, Al Omar A (2008) Characterization of deformation stability of medium carbon microalloyed steel during hot forging using phenomenological and continuum criteria. J Mater Process Technol 199:140–149. doi:10.1016/jjmatprotec200708004

11. Xu L, Wang C, Liu G, Bai B (2009) Hot deformation behavior of medium carbon V-N microalloyed steel. Trans of Nonferr Met Soc China 19:1389–1394. doi:10.1016/S1003-6326(09)60038-8

12. Wei H, Liu G (2014) Effect of Nb and C on the hot flow behavior of Nb microalloyed steels. Mater Des 56:437–444. doi:10.1016/jmatdes201311009

13. Stephenson DA, Agapiou JS (2005) Metal cutting theory and practice. CRC Press, Boca Raton

14. Bramfitt BL, Benscoter AO (2002) Metallographer's guide: practice and procedures for irons and steels. ASM International, Materials Park

15. Opiela M, Kamińska M (2011) Influence of the rare-earth elements on the morphology of non-metallic inclusions in microalloyed steels. J Achiev Mat Manuf Eng 47:149–156

16. Xiao G, Dong H, Wang M, Hui W (2011) Effect of sulfur content and sulfide shape on fracture ductility in case hardening steel. J Iron Steel Res Int 18:58–64. doi:10.1016/S1006-706X(11)60105-2

17. Kizu T, Urabe T (2009) Hot ductility of sulfur-containing low manganese mild steels at high strain rate. ISIJ Int 49:1424–1431

18. Prasad YVRK, Gegel HL, Doraivelu SM, Malas JC, Morgan JT, Lark KA, Barker DR (1984) Modeling of dynamic material behavior in hot deformation-forging of Ti-6242. Metall Trans A 15:1883–1892. doi:10.1007/BF02664902

19. Lenz M, Gall S, Schmack F, Mayer HM, Reimers W (2014) Hot working behavior of a WE54 magnesium alloy. J Mater Sci 49:1121–1129. doi:10.1007/s10853-013-7790-y

20. Quan G, Zhao L, Chen T, Wang Y, Mao Y, Lv W, Zhou J (2012) Identification for the optimal working parameters of as-extruded 42CrMo high-strength steel from a large range of strain, strain rate and temperature. Mater Sci Eng A 538:364–373. doi:10.1016/jmsea201201062

21. Liu Y, Ning Y, Yao Z, Guo H, Nan Y (2014) Effect of true strains on processing map for isothermal compression of Ni-200Cr-25Ti-15Nb-10Al Ni-base superalloy. J Alloys Compd 612:56–63. doi:10.1016/jjallcom201405165

22. Murty SVS Narayana, Rao BN, Kashyap BP (2005) Identification of flow instabilities in the processing maps of AISI 304 stainless steel. J Mater Process Technol 166:268–278. doi:10.1016/jjmatprotec200409089

23. Murty SVSN, Rao BN (1998) On the development of instability criteria during hotworking with reference to IN 718. Mater Sci Eng A 254:76–82. doi:10.1016/S0921-5093(98)00764-3

24. Sneddon IN, Hill R, Naghdi PM, Ziegler H (1963) Progress in solid mechanics. North-Holland Publishing Company, New York

25. Srinivasan N, Prasad YVRK (1994) Hot-working characteristics of nichrome and the development of a processing map. J Mater Process Technol 41:409–424. doi:10.1016/0924-0136(94)90005-1

26. Ma XO, Zeng WD, Sun Y, Zhao YQ, Wang SL, Zhou YG (2010) A Comparative study of various flow instability criteria in processing map. Rare Met Mater Eng 39:756–761. doi:10.1016/S1875-5372(10)60096-3

27. Xu YM, Weins WN, Dhir A (1993) A metallographic investigation of banding and diffusion of phosphorus in steels. Metallogr Characteriz Met Weld Process Serv 20:457–470

28. Lin YC, Chen MS, Zhong J (2008) Microstructural evolution in 42CrMo steel during compression at elevated temperatures. Mater Lett 62:2132–2135. doi:10.1016/jmatlet200711032

29. Sun L, Muszka K, Wynne BP, Palmiere EJ (2014) Effect of strain path on dynamic strain-induced transformation in microalloyed steel. Acta Mat 66:132–149. doi:10.1016/j.actamat.2013.11.062

30. Jorge-Badiola D, Gutierrez I (2004) Study of the strain reversal effect on the recrystallization and strain induced precipitation in a Nb-microalloyed steel. Acta Mat 52:333–341. doi:10.1016/j.actamat.2003.09.018

31. Ozturk F, Polat A, Toros S, Picu RC (2013) Strain hardening and strain rate sensitivity behaviors of advanced high strength steels. Iron Steel Res Int 20:68–74. doi:10.1016/S1006-706X(13)60114-4

32. Cyril N, Fatemi A, Cryderman R (2009) Effects of sulfur level and anisotropy of sulfide inclusions on tensile, impact, and fatigue properties of SAE 4140 steel. SAE Int Mater Manuf 1(1):218–227. doi:10.4271/2008-01-0434

33. Lunev VV, Pirozhkova VP (2012) Nature and diagnostics of nonmetallic inclusions in steels. Russ Metall 6:535–538. doi:10.1134/S0036029512060122

34. Shevtsova OA, Zyuban NA, Rutskii DV (2011) Aspects of the formation of sulfide inclusions and their effect on the quality of low-alloy structural steels. Metall 54:839–844. doi:10.1007/s11015-011-9382-x

35. Ma J, Zhang B, Xu DK, Han EH, Ke W (2010) Effects of inclusion and loading direction on the fatigue behavior of hot rolled low carbon steel. Int J Fatigue 32:1116–1125. doi:10.1016/jijfatigue200912005

36. Luo CH (2001) Evolution of voids close to an inclusion in hot deformation of metals. Comput Mater Sci 21:360–374. doi:10.1016/S0927-0256(01)00149-5